Geofísica Internacional (2025) **64-4**: 1833- 1845

Resolution of four collinear arrays to a 3D prism in multi-electrode resistivity surveys

Félix Aguilar[1,2] and Carlos Flores[1]*

Abstract

The Earth Resistivity Tomography (ERT) is a geophysical technique widely used in many areas such as hydrogeology, mining, geothermal, and archeology applications. This method usually employs standard electrode arrays. Here, we examine the performance of four of these arrays (Wenner (WN), dipole-dipole (DD), pole-pole (PP), and pole-dipole (PD)) by analyzing their resolutions of the parameters of a simple three-dimensional (3D) prism embedded in a homogeneous host. The five model parameters are depth, length, width, thickness, and resistivity. We consider different versions of a base model by varying their five parameters. Sensitivities associated with the derivatives of the apparent resistivity response with respect to the parameters are weighted by the data errors. These errors are estimated considering a power law function for the error in the measured voltages. Parameter uncertainties are estimated performing a singular value decomposition of the sensitivity matrices. The best resolved parameters are the depth to top and length of the body, while the least resolved are the resistivity, width and thickness. The results show that the number of data is the most critical factor influencing the resolution of the prismatic body. The pole-dipole array is the best of the four arrays because it had more data, better than the Wenner array, despite having higher sensitivities. Another option with a larger number of data is the Schlumberger array with arbitrary separation between potential electrodes.

Key words: electrical resistivity tomography, electrode arrays, parameter resolution.

Resumen

La Tomografía de Resistividad Eléctrica (TRE) es una técnica geofísica ampliamente usada en diferentes aplicaciones como la hidrogeología, minería, geotermia y arqueología. En este método generalmente se usan arreglos convencionales de electrodos. Aquí examinamos el desempeño de cuatro de estos arreglos (Wenner (WN), dipolo-dipolo (DD), polo-polo (PP) y polo-dipolo (PD)) analizando sus resoluciones a los parámetros de un prisma tri-dimensional (3D) inmerso en un medio huésped homogéneo. Los cinco parámetros del modelo son profundidad, longitud, ancho, espesor y resistividad. Al variar sus cinco parámetros se consideran versiones diferentes de un modelo base. Las sensibilidades, asociadas con las derivadas de la respuesta de resistividad aparente con respecto a los parámetros, son ponderadas con los errores de los datos. Estos errores se estimaron con una ley de potencia de los errores en los voltajes. Las incertidumbres de los parámetros se estiman con una descomposición en valores singulares de las matrices de sensibilidad. Los parámetros mejor resueltos son la profundidad a la cima y la longitud del cuerpo, los peor resueltos son la resistividad, el ancho y el espesor. Los resultados muestran que el número de datos es el factor más importante en la resolución del cuerpo prismático. De los cuatro arreglos, el polo-dipolo fue el mejor porque fue el arreglo con más datos, aún mejor que el Wenner, que tuvo sensibilidades mayores. Otra opción con un número alto de datos es el arreglo Schlumberger con una separación arbitraria entre electrodos de potencial.

Palabras clave: tomografía de resistividad eléctrica, arreglos electródicos, resolución de parámetros.

Received: November 22, 2024; Accepted: Julio 31, 2025; Published on-line: October 1, 2025.

Editorial responsibility: Dr. Alfredo Trujillo Alcántara

* Corresponding author: Carlos Francisco Flores-Luna, cflores@cicese.mx

[1] Centro de Investigación Científica y Educación Superior de Ensenada, Departamento de Geofísica Aplicada. Carretera Ensenada-Tijuana Núm. 3918, Zona Playitas, Ensenada, Baja California, México 22860.

[2] Universidad Autónoma del Carmen, Campus III, Facultad de Ingeniería, , Av. Central s/n, Cd. Del Carmen, Campeche, México 24115. felixaguilarcr7@gmail.com

Félix Aguilar Cruz, Carlos Francisco Flores-Luna

https://doi.org/10.22201/igeof.2954436xe.2025.64.4.1841

1. Introduction

Electrical Resistivity Tomography (ERT) is a geophysical method used to estimate the subsurface electrical resistivity from measurements made at the surface. Over the recent years, the use of ERT has experienced a significant increase in diverse applications such as hydrogeology, geotechnical, and environmental studies (e.g., Chambers et. al., 2006; Adeoti *et al.*, 2017; Gūndoğdy *et al.*, 2020). This progress has been prompted by the availability of commercial multi-electrode systems and efficient two- and three-dimensional (2D and 3D) inversion programs. In a multi-electrode survey all the electrodes are separated at a constant distance along a profile; data measurement is carried out with a micro-processor controlled system that commands which electrodes function as current sources and which operate as potential probes.

There are many possible ways to arrange the electrodes in ERT (Szalai and Szarka, 2008). In the last two decades, several works have emphasized the advantages of using optimized arrays to improve the resolution of the subsurface structure (Furman *et al.*, 2003; Stummer *et al.*, 2004; Wilkinson *et al.*, 2006; Nyquist *et al.*, 2007; Blome *et al.*, 2011; Wilkinson *et al.*, 2012). An optimized data set is designed to include conventional and unconventional electrode distribution; the so-called comprehensive array is the best optimized electrode arrangement that incorporates the totality of all possible configurations. The total four-electrode apparent resistivities in a comprehensive dataset is $n(n-1)(n-2)(n-3)/8$, where n is the number of electrodes in the layout. For our example of 14 electrodes this results in 3,003 apparent resistivities, which is a large number of data. In these optimized layouts a trade-off is searched between resolution and cost, the latter associated with long measurement times and the convenience of reducing the effect of induced polarization between measurements (Dahlin, 2000). One shortcoming of the optimized approach is that it requires the calculation of the sensitivities in a 2D model, a time consuming tool not easily accessible to everyone.

The present work analyzes four collinear arrays that are commonly used. They are the Wenner (WN), dipole-dipole (DD), pole-dipole (PD), and pole-pole (PP) arrays. The last two configurations are ideal; in the PP array one current and one potential electrode are located at infinity, and in the PD array one of the current electrodes is also positioned at infinity. In the actual field practice we need at least four electrodes to define an apparent resistivity. Then, the ideal ¨at infinity¨ electrodes are replaced here by ¨far¨ electrodes, positioned at a large but finite distance, avoiding then the associated errors (Razafindratsima *et al.*, 2014; Xiao *et al.*, 2015). Figure 1 shows the geometry of the four arrays, where the usual notation for the current (A and B) and potential (M and N) electrodes is used. These arrays are characterized by a set of distances such as the dipole length *¨a¨*, the dipole separation factor *¨n¨* (usually an integer value), and *L*. This characteristic length is the distance between the two outermost active electrodes (disregarding the far electrodes).

When planning an ERT survey a frequently asked question is, which array should one use to obtain the maximum amount of subsurface information given a finite number of multi-electrode positions? This question is difficult because many factors might affect an array's performance in a particular application. Ward (1990) proposed a qualitative grading for several arrays based on fourteen factors, which can be summarized into: a) the depth of investigation, b) the resolution to both horizontal and vertical changes of the subsurface resistivity, c) the effect of noise, and d) the horizontal data coverage (Loke, 2011). Numerous works have addressed one or more of these aspects by studying the merits and limitations of different electrode configurations. Among these are analog models (Apparao *et al.*, 1992; Apparao *et al.*, 1997), numerical modeling of simple 2D or 3D inhomogeneities (Van Nostrand, 1953; Coggon, 1973; Dey *et al.*, 1975; Militzer *et al.*, 1979; Brass *et al.*, 1981), and smooth-constrained inversions of synthetic data (Beard and Tripp, 1995; Oldenburg and Li, 1999; Dahlin and Zhou, 2004; Gharibi and Bentley, 2005; Okpoli, 2013).

Physical insight on the depth of investigation and the vertical resolution can be gained from the depth of investigation characteristic (DIC) proposed by Roy and Apparao (1971). This function describes how a thin layer in a homogeneous half-space contributes to the measured voltage at the surface; they are shown in Figure 2a for our four arrays, using a characteristic length of 6 units. They are normalized by the total potential at the surface. These curves start from zero at the surface, reach a maximum at a certain depth, and decay for larger depths. The WN array has its peak at the shallowest depth with a sharp curve, indicating that its depth of investigation is the shallowest but it has the best vertical resolution of the four arrays. On the contrary, the PP array has the maximum depth of investigation but lowest vertical resolution due to a flatter curve. Also shown with thick lines are the median depths of Edwards (1977), the depth at which the integral of the DIC function from the surface to the median depth is the same as from the median depth to infinity. The median depth is the measure most used of the DIC in practice.

Signal contribution sections are the extension to 2D (Loke and Barker, 1995) or 3D (Barker, 1979). Figure 1 shows the 3D signal contribution sections (Loke and Barker, 1995) for a homogeneous half-space calculated for a characteristic length of 6 units for the four arrays. They give the relative contributions by individual 3D volume elements to the total potential measured by the two potential electrodes. These sections share the feature of having zones of positive and negative contributions. They are helpful for a homogeneous earth, but they might be limited

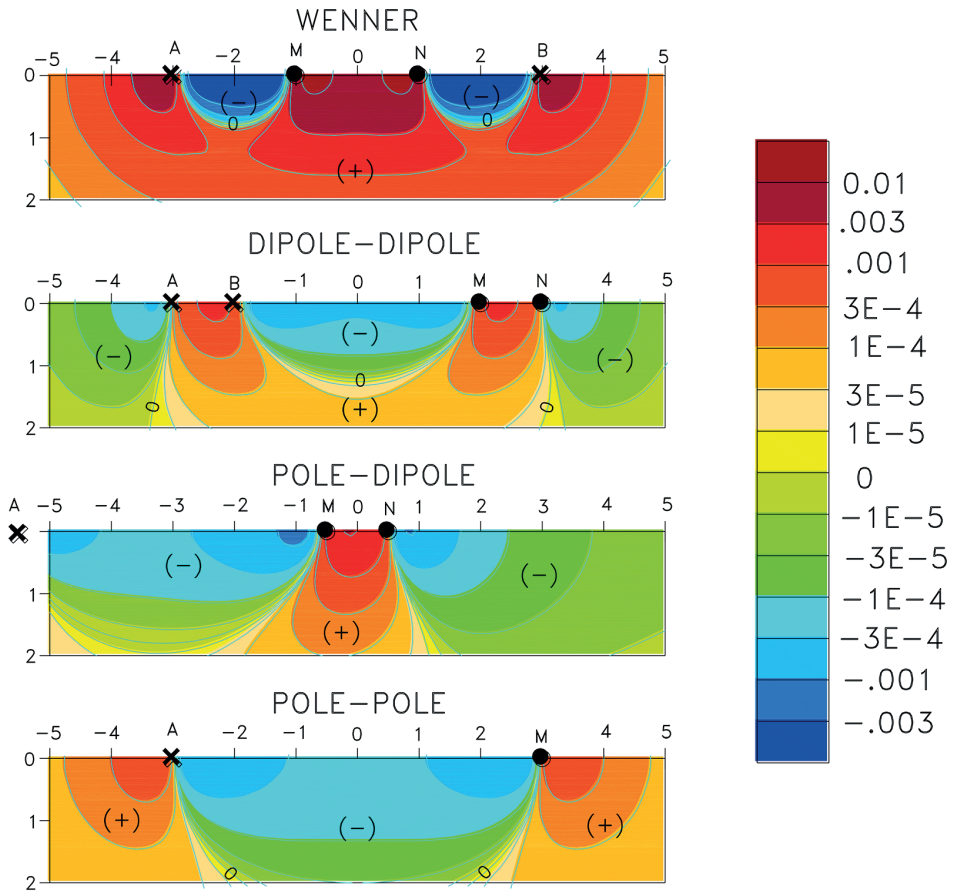

Figure 1. Signal contributions in a homogeneous 3D half-space by the Wenner (WN), dipole-dipole (DD), pole-dipole (PD), and pole-pole (PP) arrays. The far-electrodes of PD and PP are located at large but finite distances from the nearby electrodes. The contours (in V/m^3) indicate the signal contributions to the measured surface voltages of volume elements for a characteristic length of six length units.

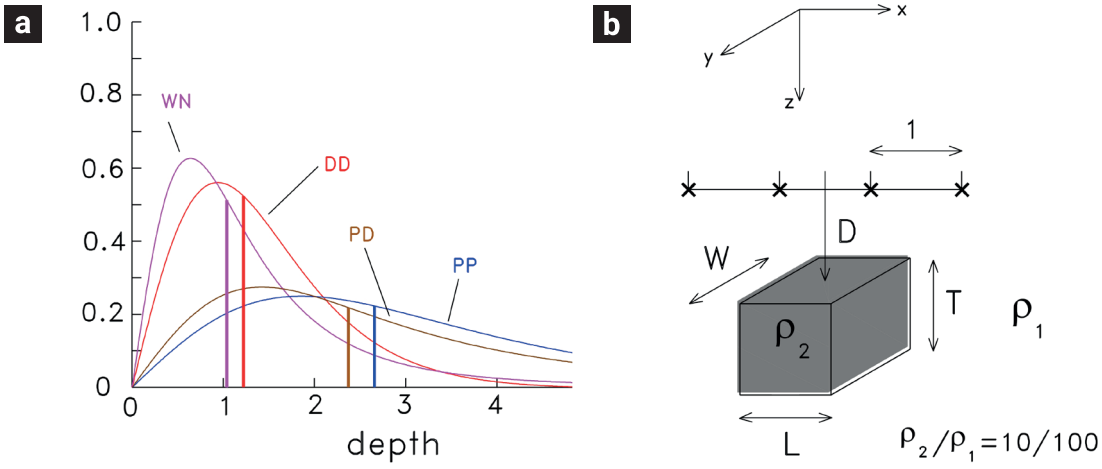

Figure 2. a) Normalized Depth of Investigation Characteristic (DIC) of the four arrays for a characteristic length of 6 units. Wenner (WN), dipole-dipole (DD), pole-dipole (PD), and pole-pole (PP) arrays. The horizontal axis is the depth in unit lengths. The vertical bars indicate the effective depths. b) Base model of a single prismatic inhomogeneity embedded in a homogeneous half-space of 100 Ωm. The depth to top (D), length (L), width (W), and thickness (T) are all one unit length.

in assessing the resolution of a non-homogeneous subsurface. The shape and intensity of these contours will be perturbed by any heterogeneity, as shown by a 2D body by Dey *et al.*, (1975) or by Gómez-Treviño and Esparza, (2013) for the case of a stratified medium.

To evaluate the performance of each one of the four arrays, we calculate the sensitivities of the parameters of several prismatic models which are perturbed versions of a base model. These sensitivities are weighted by the expected errors in the apparent resistivities, which are estimated by a power noise law in the voltages. The correlation between parameters is considered by performing a singular value decomposition (SVD) analysis of the sensitivity matrix, giving estimates of the uncertainty in the model parameters. With this approach we evaluate which are the best resolved parameters of the models and recommend the arrays with the best global performance.

2. Method

The base model is a simple 3D conductive prismatic body defined by five parameters (Figure 2b): depth to top (D), length (L), width (W), thickness (T), and resistivity (ρ_2=10 Ωm). The host is a 100 Ωm homogeneous half-space. The depth, length, width, and thickness are all one unit length. The surface electrodes of any array are also separated one unit length or any integer multiple of this distance. In this way, the calculated responses are scale independent, i.e. the same response is obtained if this unit length is 1 m or 30 m, as long as the body dimensions are accordingly scaled. We used 14 surface electrode positions aligned on a profile passing over the central part of the anomalous body. The arrays were designed to simulate a common practice in tomographic data acquisition by considering the maximum number of apparent resistivities that can be measured with this number of electrodes. Figure 3 shows the positions of the current and potential electrodes considered for each array. The pseudosection points are also shown, where the median depths of Edwards (1977) were used for the pseudodepths. It is worth noting that the pseudosections are used for display purposes, they do not represent the earth volume that is contributing to the associated apparent resistivity. The "at infinite" electrodes of the PD and PP arrays were positioned at relatively large distances; the B current electrode of the PD and PP arrays at x=-13 and the N potential electrode of the PP array at x=26 length units. Notice the different number of apparent resistivities that can be measured with each array: 26, 95, 137, and 91 for the WN, DD, PD, and PP arrays, respectively.

Each array is evaluated by assessing how well the five parameters of a series of models are resolved. The various models considered are variations of the base model where only one of the five parameters is varied, keeping constant the other four. Parameter resolution is evaluated in a two-step process; first the sensitivities of each array to the five parameters of the model are estimated, followed by the calculation of the resolution of each parameter with a singular value decomposition of the sensitivity matrix. The sensitivity a_{ij} of the *ith* apparent resistivity $\rho_{a,i}$ with an error $\Delta\rho_{a,i}$ to the *jth* model parameter p_j is defined by

$$a_{ij} = \frac{p_j}{\Delta\rho_{a,i}} \frac{\partial \rho_{a,i}}{\partial p_j} \tag{1}$$

Calculating of the apparent resistivities in (1) requires knowing the voltages at a couple of potential electrodes produced by the inhomogeneous distribution of the subsurface resistivity when a pair of electrodes injects current. We used the surface integral equation method to calculate these voltages. Several authors have described and used this technique (Snyder, 1976; Spiegel *et al.*, 1980; Schulz, 1985, Das and Parasnis, 1987). The secondary potential V_S at a point with position vector $\bar{r}$ can be calculated by a surface integral of a charge distribution built up at the surface enclosing the anomalous body, given by

$$V_s(\bar{\boldsymbol{r}}) = \iint q(\bar{r'})\ G(\bar{r}, \bar{r'})\, dS \tag{2}$$

where q is the surface charge distribution and G is the half-space Green's function. The unknown surface charge is evaluated with an integral equation (Spiegel *et al.*, 1980),

$$\frac{q(\bar{r}_B)}{2\,K_{21}} = \frac{\rho_1 I}{4\,\pi}\ \hat{n}\cdot\nabla\left(\frac{1}{|\bar{r}_B-\bar{r}_s|}\right) + \frac{1}{4\pi}\int_{B'}\int q(\bar{r}_{B'})\, n\cdot\nabla\left(\frac{1}{|\bar{r}_B-\bar{r}_{B'}|}\right) d^2\bar{r}_{B'} \tag{3}$$

where $\bar{r}_B$ and $\bar{r}_{B'}$ are the position vectors of two different points of the enclosing surface, $K_{21}=(\rho_2-\rho_1)/(\rho_2+\rho_1)$ with ρ_1 and ρ_2 the resistivities of the host and anomalous body, respectively, I is the source current intensity, and $\hat{n}$ the unit vector normal to the surface. To compute this equation numerically, the surface is divided into N cells of area Δ^2 and considering a constant charge within each cell. The resulting equation is

$$q_i\left[1+\frac{K_{21}\,\Delta^2}{2\,\pi}\frac{\cos\gamma_{i\,s*}}{|\bar{r}_i-\bar{r}_s^*|^2}\right]+\frac{K_{21}\,\Delta^2}{2\,\pi}\sum_{j=1}^{N} q_j\left[\frac{\cos\gamma_{i\,j}}{|\bar{r}_i-\bar{r}_j|^2}+\frac{\cos\gamma_{i\,j*}}{|\bar{r}_i-\bar{r}_j^*|^2}\right] = \frac{-\rho_1 K_{21} I}{2\,\pi}\left[\frac{\cos\gamma_{i\,s}}{|\bar{r}_i-\bar{r}_s|^2}+\frac{\cos\gamma_{i\,s*}}{|\bar{r}_i-\bar{r}_s^*|^2}\right]\quad i=1,\cdots N \tag{4}$$

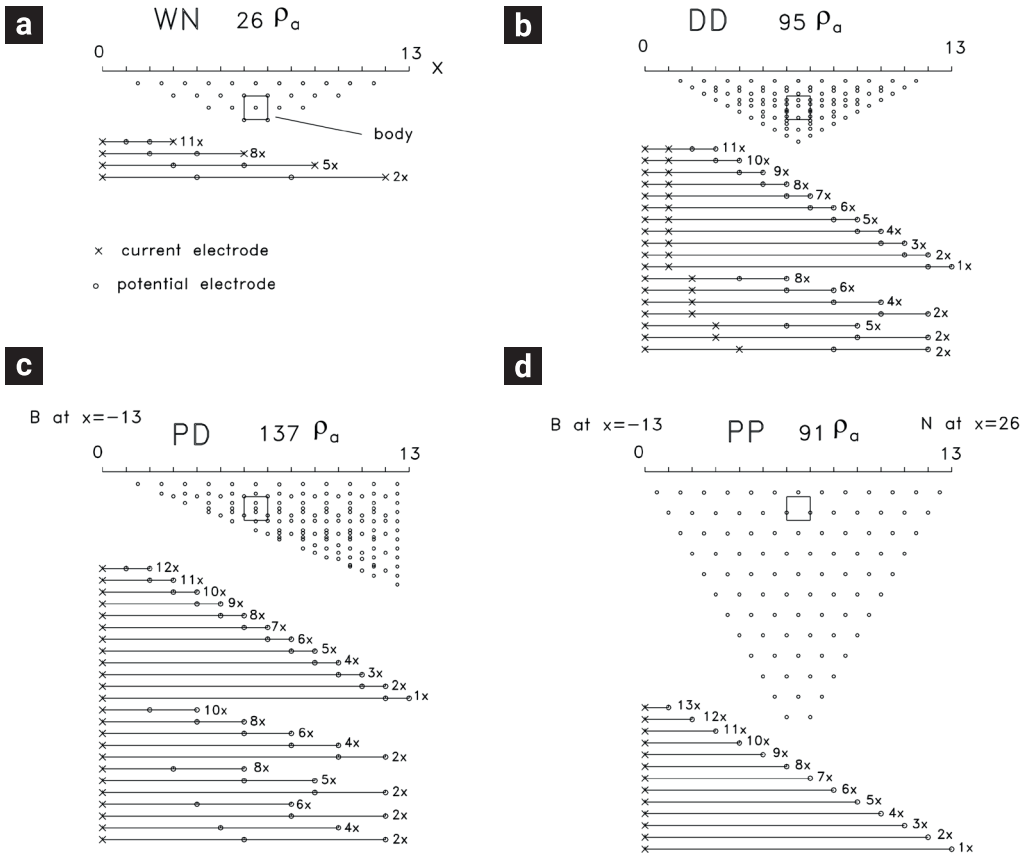

Figure 3. Electrode layouts for the four arrays. a) WN (Wenner), b) DD (dipole-dipole), c) PD (pole-dipole), and d) PP (pole-pole). The location of the plotting points of the pseudosections are shown together with the base model as a reference and the number of apparent resistivity measurements. The notation 11x means that the indicated electrode geometry repeats 10 times to the right with one unit length shifts

where γ_{ij} is the angle between the normal vector at the center of the ith cell and the vector $\bar{r}_i - \bar{r}_j$, the asterisk denotes the image source about the air-earth interface, and the sum excludes the singularity at $i=j$. This can be expressed in matrix notation as $\boldsymbol{A}\,\boldsymbol{q}=\boldsymbol{s}$, where the matrix $\boldsymbol{A}$ contains the geometrical relationships between the electric fields at the cells, $\boldsymbol{q}$ the surface charge at the N cells, and $\boldsymbol{s}$ the electric fields imposed by the current source. The system of linear equations is solved by Gaussian elimination. After knowing the values of the surface charge in each cell, the total potential at the *kth* receiver is

$$V_k = \frac{\rho_1 I}{2\pi}\,\frac{1}{|r_i - r_s|} + \frac{\Delta^2}{4\pi}\sum_{i=1}^{N} q_i \left(\frac{1}{|\bar{r}_k - \bar{r}_i|} + \frac{1}{|\bar{r}_k - \bar{r}_i^*|}\right) \tag{5}$$

Finally, the apparent resistivities were calculated with

$$\rho_a = \frac{K}{I}\,(V_{AM} - V_{AN} - V_{BM} + V_{BN}) \tag{6}$$

where K is the geometric factor of the array, and the four total voltages are those produced by the two current electrodes A and B at the potential electrodes M and N.

The voltages and apparent resistivities were calculated with a program constructed in MatLab and run at the LAMB cluster of CICESE. To reduce the influence of the cell discretization on the voltage responses we used square cells of dimensions 0.05 by 0.05 units for all models. The numerical procedure was tested for convergence (Aguilar Cruz, 2019) and successfully compared with a published response generated by Pridmore *et al.* (1981) with another method.

Regarding the errors in the apparent resistivities, $\Delta\rho_{a,i}$ in expression (1), we adopted the approach proposed by Zhou and Dahlin (2003). Using the reciprocity principle, they estimated the voltage errors in thousands of measured voltages of nine different survey areas with multi-electrode layouts for the dipole-dipole, Wenner and Schlumberger arrays. They modeled the fractional error as the following sum of a power law plus a random component,

$$\frac{\varepsilon}{V} = \left(\frac{\alpha}{V}\right)^{\beta}\,(1+R) \tag{7}$$

where ε is the voltage error, V is the voltage, α and β are constants that define the power law, and R is a random number. When plotted in a log-log scale the power law transforms into a straight line. Figure 4 shows the nine lines estimated by least squares by these authors, where a high variability is evident. In this work we considered the average of these straight lines ($\alpha = 0.014$, $\beta = 0.552$), as shown with a dashed line in Figure 4, to simulate the errors in the calculated voltages. The same power law was applied to the voltages of all arrays. For the final results it is not important which power law is adopted, as long as it is the same for all the models. As the noise depends on the intensity of the voltages, and these in turn depend on the intensity of the injected current, we assumed a common current of 0.1 A for all the models.

After the sensitivities are calculated, the uncertainties in the parameters are estimated with a Singular Value Decomposition (SVD) of the Jacobian or sensitivity matrix. To briefly describe this method, consider that any variation of the base model is specified by the parameters p_j, $j = 1,..., N$ with N = 5. The apparent resistivities are denoted by $y_i, i = 1..., M$. By linearization, the expected changes in the response dy_i produced by small variations in the parameters are given by

$$dy_i = \sum_{j=1}^{N} a_{ij}\, dp_j \qquad i = 1, \ldots, M \tag{8}$$

or in matrix notation $d\mathbf{y} = \mathbf{A}\, d\mathbf{p}$. The elements a_{ij} of the sensitivity matrix $\mathbf{A}$ are defined by expression (1).

The sensitivity matrix is decomposed using the SVD technique, giving

$$\mathbf{A} = \mathbf{U}\mathbf{S}\mathbf{V}^T \tag{9}$$

where T stands for transpose, $\mathbf{U}\,(M \times N)$ and $\mathbf{V}\,(N \times N)$ are the eigendata and eigenparameter matrices, and $\mathbf{S}\,(N \times N)$ is a diagonal matrix containing the singular values. Edwards, *et al.*, (1981) showed that the errors in the eigenparameters, defined by $d\mathbf{p}^* = \mathbf{V}^T d\mathbf{p}$, are $1/S_{jj}$, the reciprocal of the corresponding singular value. The uncertainties or error bounds of the model parameters (Raiche *et al.*, 1985) are given by

$$p_j^{\pm} = p_j\, exp\left(\pm B_j\, \beta\right) \tag{10}$$

with

$$B_j = \left[\sum_{k=1}^{N} \left(\frac{V_{jk}}{s_k}\right)^2\right]^{1/2} \tag{11}$$

where $p_j^{\pm}$ are the upper and lower bounds of a 68 % confidence level for the parameter p_j, V_{jk} are the coefficients of the eigenparameter matrix, s_k are the singular values, and β is a measure of the misfit error. As we are not doing any inversion, an arbitrarily value of unity was assigned to β. In this approach, poorly resolved parameters usually give unrealistic large values of the model errors.

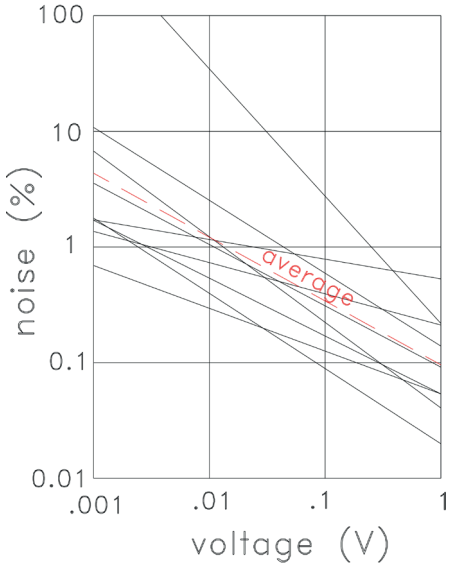

Figure 4. Linear fits to the log percent error vs log voltage estimated by Zhou and Dahlin (2003) in nine resistivity surveys. The average relation used in this work is denoted with dashed line.

3. Results

Instead of showing the sensitivity values for every apparent resistivity, the results for every array and parameter are presented in terms of the mean squared sensitivity, given by

$$A_j = \sqrt{\sum_{i=1}^{M} a_{i,j}^2 / M} \tag{12}$$

where M is the number of apparent resistivities. The mean parameter sensitivities of the four arrays using the layouts of Figure 3 are depicted in Figures 5 to 9. According to the definition in expression (1), the sensitivities in these figures are dimensionless. Figure 5 corresponds to depth variations of the base model, keeping the other four parameters fixed and unperturbed. We considered depth values of 0.1, 0.2, 0.5, 1, and 2 length units (Figure 5a). The mean sensitivities of the five parameters (depth (D), length (L). width (W), thickness (T) and body resistivity (ρ_2) at these depths are shown in Figure 5b using log-log plots. As the depth increases from 0.1 to 2 units the sensitivities of the five parameters decrease. The exception to this behavior are the sensitivities of the depth, which peak at about 0.3 or 0.5 units; some of these depths resemble the DIC (Depth of Investigation Characteristic) of Figure 2a for a homogeneous earth. The WN and PP arrays have the highest and lowest average sensitivity values.

The cases when the length of the body in the x-direction has the values 0.5, 1, 5, 9, and 13 units are depicted in Figure 6. As this parameter grows the sensitivities of the five parameters increase (Figure 6b); the rate of change for short lengths is higher than for the long lengths (9 and 13 units). The clear decrease in the length sensitivity when the body is 13 units long occurs when the body edges reach the start and end of the electrode layout, which spreads from x=0 to x=13 (Figure 3).

The effects of varying the width´s body are detailed in Figure 7. The sensitivities grow as the width increases from 0.5 to 13 units (Figure 7b). They increase fast for small widths, occurring the opposite for large widths. The exception to this general behavior is the sensitivity to the width itself, it reaches a maximum value when W is about five units. This means that the volume of influence extends about 2.5 units off the profile in the y-direction. When the lateral edges of the body extend beyond this value the sensitivities decrease. Sensitivities of the depth, length, width and resistivity show a growing trend when the body thickens (Figure 8), but this trend practically flattens for large thicknesses. Thickness sensitivities slightly increase for the PP and PD arrays up to T=3, while the WN and DD arrays decrease beyond T=1. Again, this behavior qualitatively

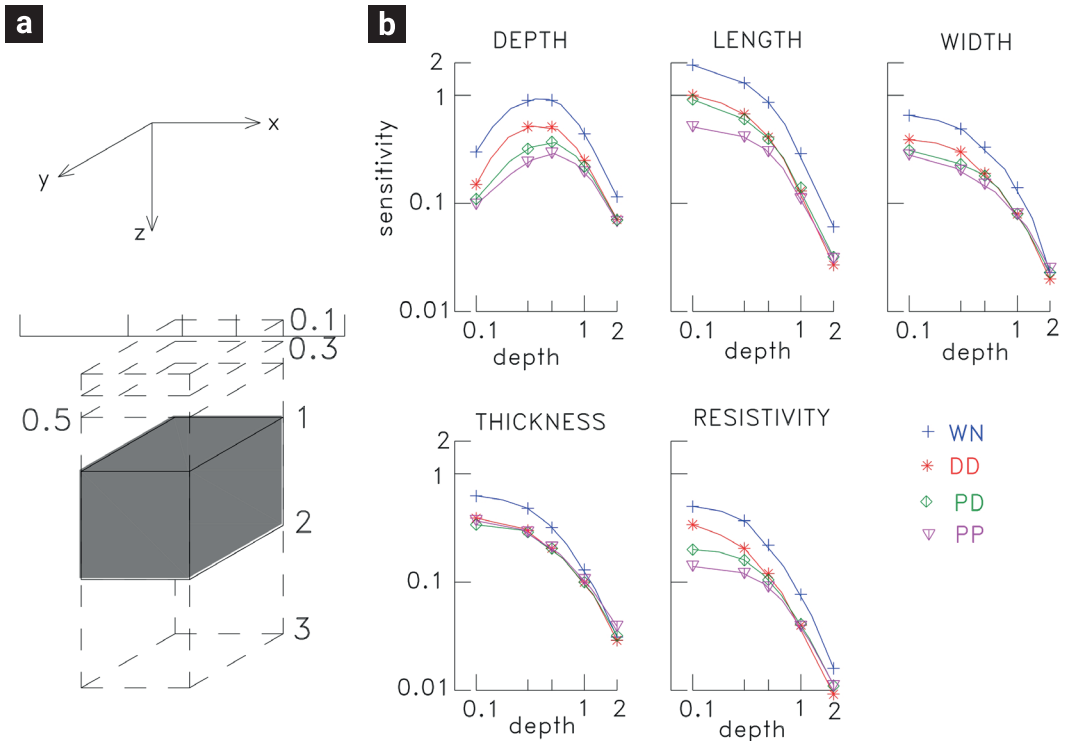

Figure 5. a) Variation of the depth of the base model, b) Mean sensitivities (dimensionless) of the five parameters. Arrays: Wenner (WN), dipole-dipole (DD), pole-dipole (PD), and pole-pole (PP).

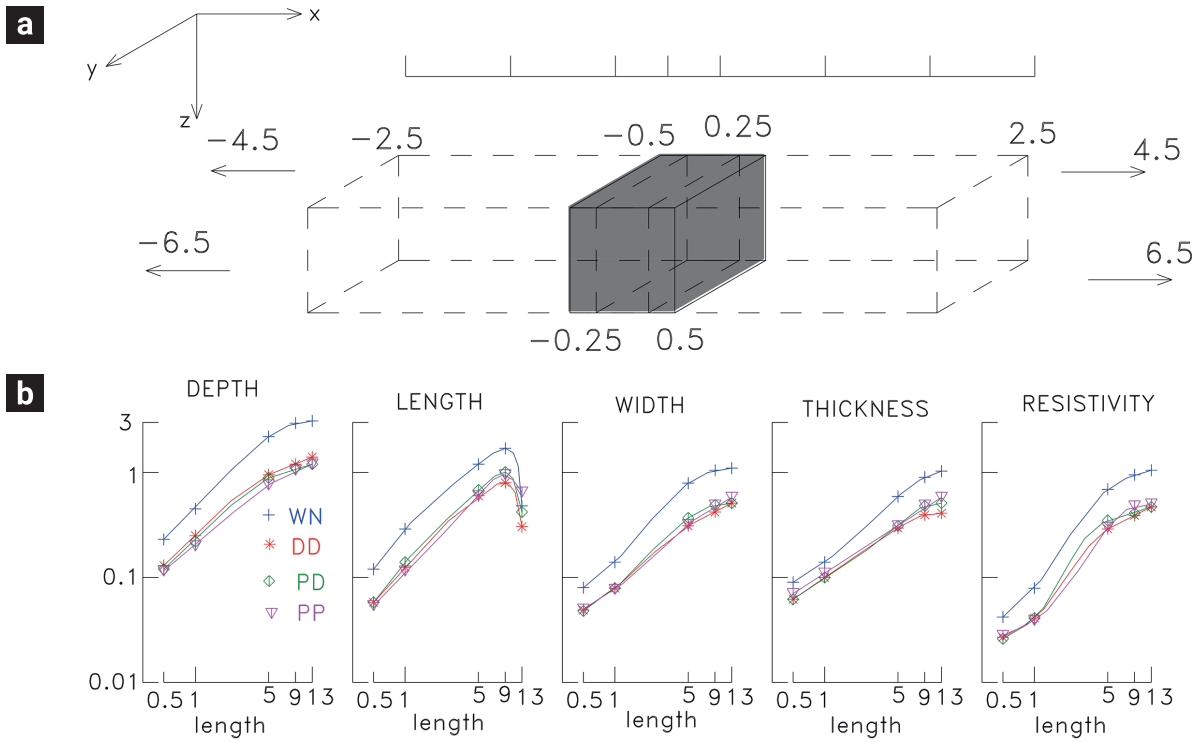

Figure 6. a) Variation of the length of the base model, b) Mean sensitivities of the five parameters. Arrays: Wenner (WN), dipole-dipole (DD), pole-dipole (PD), and pole-pole (PP).

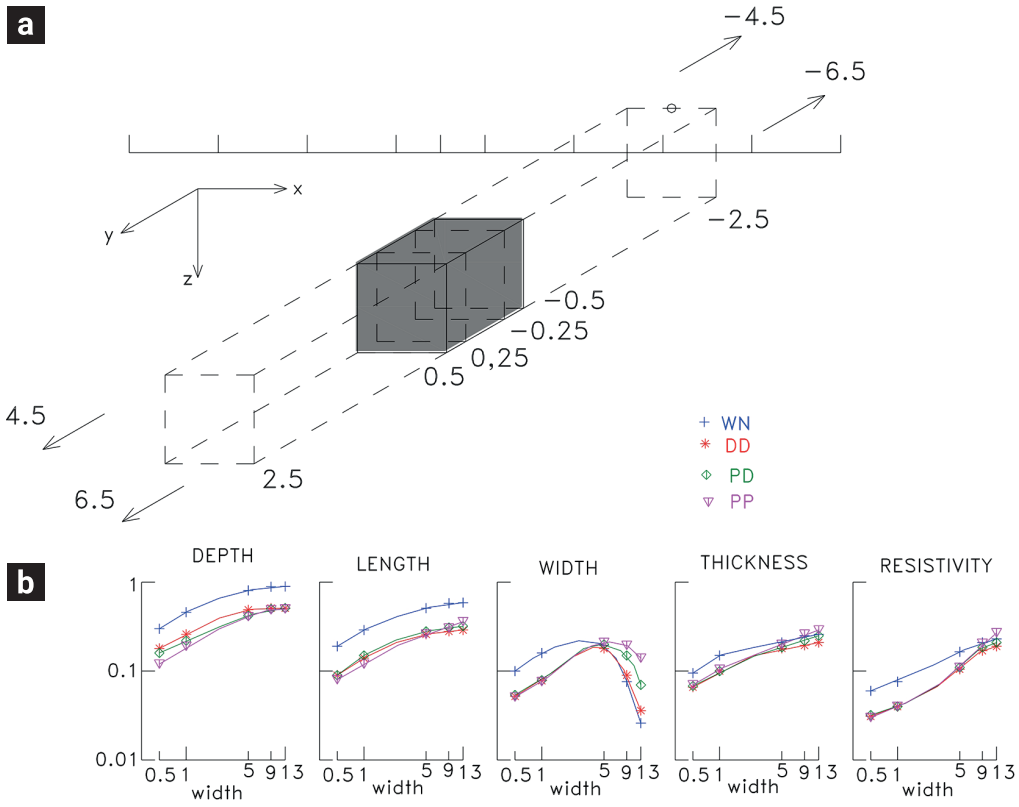

Figure 7. a) Variation of the width of the base model, b) Mean sensitivities of the five parameters. Arrays: Wenner (WN), dipole-dipole (DD), pole-dipole (PD), and pole-pole (PP).

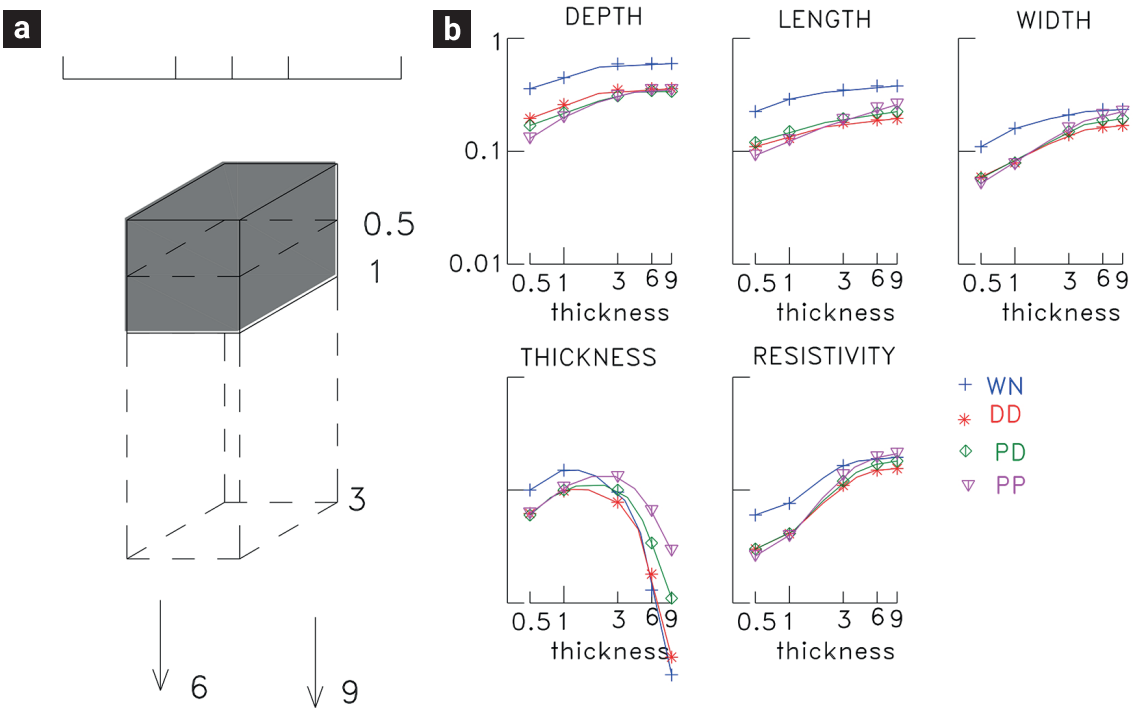

Figure 8. a) Variation of the thickness of the base model, b) Mean sensitivities of the five parameters. Arrays: Wenner (WN), dipole-dipole (DD), pole-dipole (PD), and pole-pole (PP).

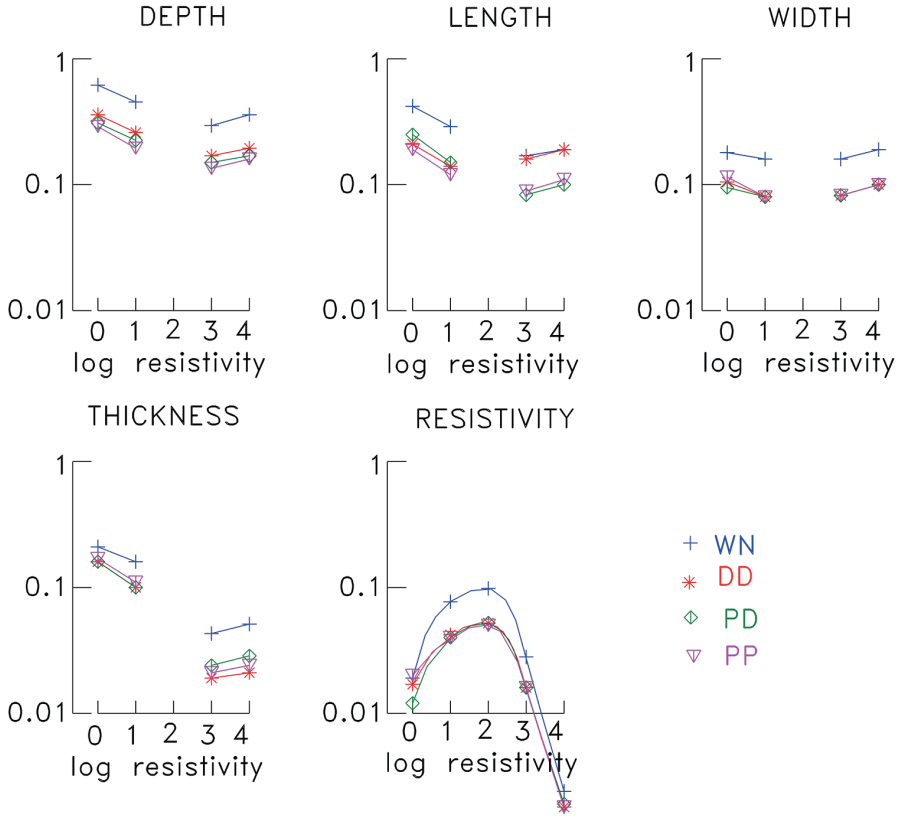

Figure 9. Mean sensitivities of the five parameters when the body resistivity is varied. Arrays: Wenner (WN), dipole-dipole (DD), pole-dipole (PD), and pole-pole (PP).

agrees with the Depth of Investigation Characteristic of Figure 2a, where the maxima of the PP and PD lie at greater depths than those of the WN and DD arrays.

The calculated sensitivities when the body resistivity (ρ_2) is varied are shown in Figure 9. Values considered for this parameter were from highly conducting (1 Ωm) to highly resistive (10,000 Ωm), keeping the host resistivity unchanged at 100 . The sensitivities of depth, length, width, and thickness decrease when the body resistivity approaches 100 Ωm, i.e., when the resistivity contrast diminishes. When the body has the same resistivity of the host medium the body obviously no longer exists, making the sensitivities to all these four parameters tend to zero; in this case the sensitivity to ρ_2 simply is the value of a homogeneous half-space. The sensitivities to *D*, *L*, *W*, and *T* show two additional features. As the resistivity contrast increases the sensitivities tend to asymptotic values, reflecting the saturation phenomenon discussed by Ward (1967). Furthermore, these curves are not symmetric with respect to $\rho_2 = 100$, i.e., the conductive case has slightly greater sensitivities for reciprocal ρ_2/ρ_1 ratios, for example, 10/100 versus 1000/100 .

After the sensitivities were calculated we proceeded with an estimation of the resolution of each parameter. Figure 10 summarizes the results of the uncertainty estimates; it shows the sum of uncertainties, expressed as percentage in a logarithmic scale, of the twenty models depicted in Figures 5 to 9. This figure shows two types of results. First, it describes the order of resolution of the five parameters of the body: depth to the top (D), length (L), width (W), thickness (T) and resistivity (ρ_2). The depth is the parameter with smaller uncertainties, is the best resolved of the five body parameters. The length occupies the second place followed by the thickness. The width and resistivity are the least resolved parameters. The second aspect this figure shows is how the four arrays (Wenner (WN); dipole-dipole (DD); pole-dipole (PD) and pole-pole (PP)) perform in terms of the resolution of the body parameters; the best array is highlighted with an asterisk, the worst with a circle. The number of apparent resistivities in each array are enclosed in parenthesis. The DD array was the best for the depth estimation as its uncertainty was the lowest. Notice that the PD array was the best in the other four parameters (L, W, T, and ρ_2) and slightly behind the DD for the depth. The Wenner array resulted with the highest uncertainties in all the five parameters.

4. Discussion

It is intriguing why, if the sensitivities of the Wenner array, portrayed in Figures 5 through 9, were the greatest in almost all the cases, this is not reflected in low uncertainties. As a matter of fact, this array turned out to have the lowest resolutions of the four arrays (Figure 10). In contrast, the pole-dipole array resulted with the best resolutions in four out of the five parameters, despite having sensitivities that were not exceptionally high. The most notable difference between these two arrays is

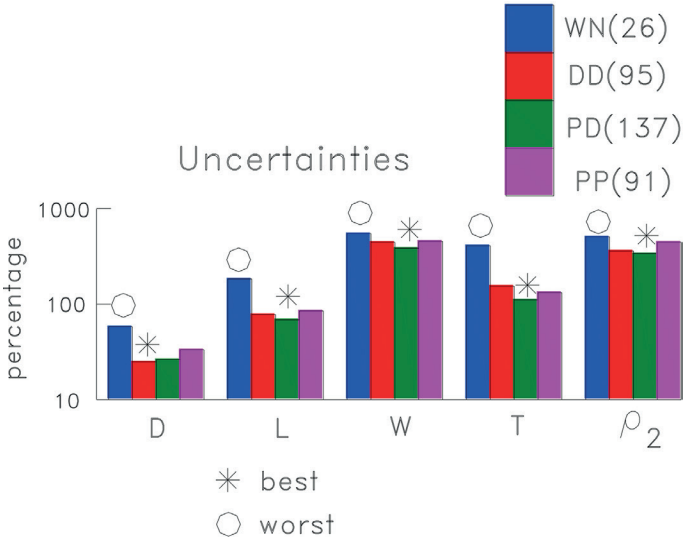

Figure 10. Sum of the uncertainties (in percent) of the twenty models considered in Figures 5 to 9 for the five body parameters (D=depth to top. L=length, W=width, T=thickness, and rho2=body resistivity) and for the four arrays (WN=Wenner, DD=dipole-dipole, PD=pole-dipole, and PP=pole-pole). The number of apparent resistivities in each array is enclosed in the parenthesis. The asterisk and circle indicate the array the lowest and greatest uncertainties, respectively.

the number of measurements. With the Wenner array only 26 measurements can be accommodated within the 14 electrode layout of Figure 3, while in the pole-dipole array, the number is 137. This suggests that the degree of resolution is not directly associated with the sensitivity of a particular array, but with the number of apparent resistivity values considered. To confirm the relevance of the data density on the resolution, we carried a similar analysis with the base model using the pole-dipole array, but now with 26 data, the same number as the Wenner array. The results of these two cases are shown in Figure 11 with the blue and green bars, where we have included the singular values of the SVD arranged in decreasing order. The sensitivities of the Wenner array are higher than those of the pole-dipole array for the five body parameters, which are reflected on lower uncertainties (except for the length). Then, with the same number of data, Wenner's higher sensitivities produce higher resolutions. Now, comparing the third block, that of PD(137) denoted with the red color, it has lower sensitivities but the singular values are higher, which results in lower uncertainties (except for the depth).

To strengthen the conclusion that the number of measurements is a critical factor in the resolution of the body parameters, we calculated the response and sensitivities with the symmetric Schlumberger array for the base model. This array maintains a small distance between the potential electrodes M and N when performing Vertical Electric Sounding. In our tomographic case, the separation between the potential electrodes does not have this restriction. Using only symmetrical four-electrode Schlumberger arrays, 161 possible measurements are made with the 14 electrodes of Figure 3. The corresponding sensitivities, singular values, and uncertainties are displayed with a brown box as SCH(161) in Figure 11. Notice that the Schlumberger sensitivities are lower than those of WN(26). However, the uncertainties are the lowest (except for the length, almost equal to PD(137)) of them all because it resulted with the highest singular values. The results of this work agree with the concept behind the optimization approach mentioned in the introduction, that the resolution improves as the data density increases, agreeing with the analysis of Stummer et.al. (2004).

Regarding the model parameters, the depth and length are usually the best resolved, with the body width and resistivity occupying the last places in resolution and the thickness in an intermediate position. Any interpreter should be aware of this resolution ordering. Although it is hard to prove, we believe actual heterogeneous resistivity distributions might alter these conclusions. Most tomography studies are inverted with smooth inversion algorithms where the horizontal and vertical variation of the subsurface resistivity is minimized. The relatively low resolution of the thickness of the anomalous body is the reason why, in many smooth inversion results, the depth to the bottom of the body is smeared down (Beard and Tripp, 1995; Loke, 2011; Dahlin and Zhou, 2004; Gharibi and Bentley, 2005). On the other hand, the low resolution of the body resistivity causes this parameter to be overestimated in smooth inversions if the body is conductive and underestimated if it is resistive.

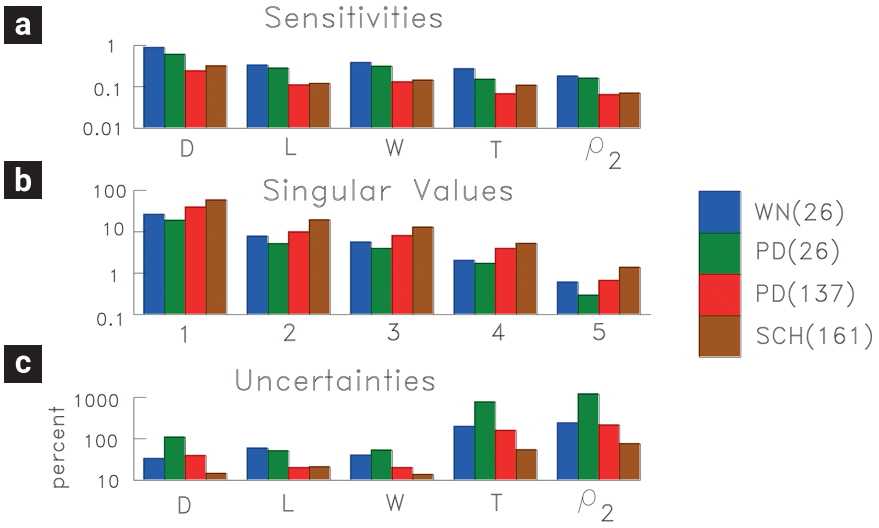

Figure 11. Comparison between the sensitivities (a), the ordered singular values (b) and uncertainties (c) of four apparent resistivity responses calculated with the Wenner (WN), pole-dipole (PD), and Schlumberger (SCH) arrays of the base model. The number of apparent resistivities used in each response are enclosed in parenthesis.

5. Conclusions

Four factors (Loke, 2011) affecting the overall performance of four commonly used electrode arrays are considered in this work. The first three (depth of investigation, horizontal and vertical resolution, and the effect of noise) are included in how the sensitivity is defined. The last one, associated with the data coverage, is dealt by comparing responses with different number of data. Other factors not considered here, such as the effect of the topographic relief, the presence of shallow heterogeneities, Induced Polarization, and the electromagnetic coupling effect produced by the wire laid on the ground. The most important factor on the global resolution of this prismatic body turned out to be the number of data. For this reason the pole-dipole array was the best. If this array cannot be used because the ¨far¨ electrode cannot be grounded due to the fixed uniform spacing between electrodes of the acquisition system, the geophysicist could alternatively use the Schlumberger array (without the restriction of the small separation between potential electrodes) as more data can be measured with this array. For a practicing geophysicist interpreting inversion results of a ERT, it should be useful to be aware that resistivity, width, and thickness of a target body are the least resolved parameters.

6. References

Adeoti, L., Afolabi, O. S., Ojo, O. A., and Ishola, S. K. (2017). Application of three electrical resistivity arrays to evaluate resolution capacity of fractured zones at Apatara Farms, Iwo, Osun State, Nigeria, *J. Appl. Sci. Environ. Management*, 21(6), 1213-1221. doi: **https://dx.doi.org/10.4314/jasem.v21i6.36**

Aguilar Cruz, F. (2019). Parameter resolution of a tri-dimensional body with several electrode arrays in the electrical resistivity technique. [*M.Sc. Thesis*], CICESE, Ensenada.

Apparao, A., Gangadhara Rao, T., Sivarama Sastry, R., and Subrahmanya Sarma, V. (1992). Depth of detection of buried conductive targets with different electrode arrays in resistivity prospecting, *Geophysical Prospecting*, 40, 749-760. doi: **https://doi.org/10.1111/j.1365-2478.1992.tb00550.x**

Apparao, A., Sivarama Sastry, R., and Subrahmanya Sarma, V. (1997). Depth of detection of buried resistive targets with some electrode arrays in resistivity prospecting, *Geophysical Prospecting*, 45(3), 365-375. doi: **https://doi.org/10.1046/j.1365-2478.1997.3360256.x**

Barker, R. D. (1979). Signal contribution sections and their use in resistivity studies, *Geophysical Journal International*, 59(1), 123-129. doi: **https://doi.org/10.1111/j.1365-246X.1979.tb02555.x**

Beard, L. P., and Tripp, A. C. (1995). Investigating the resolution of IP arrays using inverse theory, *Geophysics*, 60(5), 1326-1341. doi: **https://doi.org/10.1190/1.1443869**

Blome, M., Maurer, H., and Greenhalgh, S. (2011), Geoelectrical experimental design–Efficient acquisition and exploitation of complete pole-bipole data sets, *Geophysics*, 76(6). F15-F26. doi: **https://doi.org/10.1190/1.3511350**

Brass, G., Flathe, H., and Schulz, R. (1981). Resistivity profiling with different electrode arrays over a graphite deposit. *Geophysical Prospecting*, 29, 589-600. doi: **https://doi.org/10.1111/j.1365-2478.1981.tb00697.x**

Chambers, J. E., Kuras, O., Meldrum, P. I., Ogilvy, P. O., and Hollands, J. (2006). Electrical resistivity tomography applied to geologic, hydrogeologic, and engineering investigations at a former waste-disposal site, *Geophysics*, 71, B231-B239. doi: **https://doi.org/10.1190/1.2360184**

Coggon, J. H. (1973). A comparison of IP electrode arrays, *Geophysics*, 38(4), 737-761. **https://doi.org/10.1190/1.1440372**

Dahlin, T. (2000). Short note on electrode charge-up effects in DC resistivity data acquisition using multi-electrode arrays, *Geophysical Prospecting*., 48(1), 181-187. doi: **https://doi.org/10.1046/j.1365-2478.2000.00172.x**

Dahlin, T., and Zhou, B. (2004). A numerical comparison of 2D resistivity imaging with 10 electrode arrays, *Geophysical Prospecting*, 52(5), 379-398. doi: **https://doi.org/10.1111/j.1365-2478.2004.00423.x**

Das, U. C., and Parasnis, D. S. (1987). Resistivity and induced polarization responses of arbitrarily shaped 3-D bodies in a two-layered earth, *Geophysical Prospecting*, 35(1), 98-109. doi: **https://doi.org/10.1111/j.1365-2478.1987.tb00805.x**

Dey, A., and Morrison, H. F. (1979). Resistivity modelling for arbitrarily shaped two-dimensional structures, *Geophysical Prospecting*, 27(1), 106-136. doi: **https://doi.org/10.1111/j.1365-2478.1979.tb00961.x**

Dey, A., Meyer, W. H., Morrison, H. F., and Dolan, W. M. (1975). Electric field response of two-dimensional inhomogeneities to unipolar and bipolar electrode configurations, *Geophysics*, 40(4), 630-640. doi: **https://doi.org/10.1190/1.1440554**

Edwards, L. S. (1977). A modified pseudosection for resistivity and induced-polarization, *Geophysics*, 42(5), 1020-1036. doi: **https://doi.org/10.1190/1.1440762**

Edwards, R.N., Bailey, R.C., and Garland, G.D. (1981). Conductivity anomalies: lower crust or asthenosphere?, *Physics of the Earth and Planetary Interiors*, 25(3), 263-272. doi: **https://doi.org/10.1016/0031-9201(81)90070-4**

Furman, A., Ferré, T. P. A., and Warrick, A. W. (2003). A sensitivity analysis of electrical resistivity tomography array types using analytical element modeling, *Vadose Zone Journal*, 2(3), 416-423. doi: **https://doi.org/10.2136/vzj2003.4160**

Gharibi, M., and Bentley, L. R. (2005). Resolution of 3-D electrical resistivity images from inversions of 2-D orthogonal lines, *Journal of Environmental and Engineering Geophysics*, 10(4), 339-349. doi: **https://doi.org/10.2113/JEEG10.4.339**

Gómez-Treviño, E., and Esparza, F. J. (2013). What is the depth of investigation of a resistivity measurement? *Geophysics*, 79(2), W1-W10. doi: **https://doi.org/10.1190/geo2013-0261.1**

Gūndoğdy, N. Y., Demirci, I., Demirel, C., and Candansayar, M. E. (2020).

Characterization of the bridge pillar foundations using 3D focusing inversion of DC resistivity data, *Journal of Applied Geophysics*, 172, 103875. doi: **https://doi.org/10.1016/j.jappgeo.2019.103875**

Loke, M. H. (2011). Tutorial: 2-D and 3-D electrical imaging surveys, Geotomo Software, Malaysia.

Loke, M. H., and Barker, R. D. (1995). Least-squares deconvolution of apparent resistivity pseudosections, *Geophysics*, 60(6), 1682-1690. doi: **https://doi.org/10.1190/1.1443900**

Militzer, H., Rösler, R., and Losch, W. (1979). Theoretical and experimental investigations for cavity research with geoelectrical resistivity methods, *Geophysical Prospecting*, 27(3), 640-652. doi: **https://doi.org/10.1111/j.1365-2478.1979.tb00991.x**

Nyquist, J. E., Peake, J. S., and Roth, M. J. S. (2007). Comparison of an optimized resistivity array with dipole-dipole soundings in karst terrain, *Geophysics*, 72(4), F139-F144. doi: **https://doi.org/10.1190/1.2732994**

Okpoli, C. C. (2013). Sensitivity and resolution capacity of electrode configurations, *International Journal of Geophysics*, ID608037. doi: **https://doi.org/10.1155/2013/608037**

Oldenburg, D. W., and Li., Y. (1999). Estimating depth of investigation in dc resistivity and IP surveys, *Geophysics*, 64(2), 403-416. doi: **https://doi.org/10.1190/1.1444545**

Pridmore, D. F., Hohmann, G. W., Ward, S. H., and Sill, W. R. (1981). An investigation of finite-element modeling for electrical and electromagnetic data in three dimensions, *Geophysics*, 46(7), 1009-1024. doi: **https://doi.org/10.1190/1.1441239**

Raiche, A. P., Jupp, D. L. B., Rutter, H., and Vozoff, K. (1985). The joint use of coincident loop transient electromagnetic and Schlumberger sounding to resolve layered structures, *Geophysics*, 50(10), 1618-1627. doi: **https://doi.org/10.1190/1.1441851**

Razafindratsima, S., and Lataste, J.-F. (2014). Estimation of the error made in Pole-Dipole Electrical Resistivity Tomography depending on the location of the remote electrode: Modeling and field study, *Journal of Applied Geophysics*, 100, 44-57. doi: **https://doi.org/10.1016/j.jappgeo.2013.10.008**

Roy, A., and Apparao, A. (1971). Depth of investigation in direct current methods, *Geophysics*, 36(5), 943-959. doi: **https://doi.org/10.1190/1.1440226**

Schulz, R. (1985). The method of integral equation in the direct current resistivity method and its accuracy, Journal of Geophysics-Zeitschrift fur Geophysik, 56(3), 192-200.

Snyder, D. D. (1976). A method for modeling the resistivity and IP response of two-dimensional bodies, *Geophysics*, 41(5), 997-1015. doi: **https://doi.org/10.1190/1.1440677**

Spiegel, R. J., Sturdivant, V. R., and Owen, T. E. (1980). Modeling resistivity anomalies from localized voids under irregular terrain, *Geophysics*, 45(7), 1164-1183. doi: **https://doi.org/10.1190/1.1441115**

Stummer, P., Maurer, H., and Green, A. G. (2004). Experimental design: Electrical resistivity data sets that provide optimum subsurface information, *Geophysics*, 69(1), 120-139. doi: **https://doi.org/10.1190/1.1649381**

Szalai, S., and Szarka, L. (2008). On the classification of surface geoelectric arrays, *Geophysical Prospecting*, 56(2), 159-175. doi: **https://doi.org/10.1111/j.1365-2478.2007.00673.x**

Van Nostrand, R. G. (1953). Limitations on resistivity methods as inferred from the buried sphere problem, *Geophysics*, 18(2), 423-433. doi: **https://doi.org/10.1190/1.1437895**

Ward, S. H. (1967). Electromagnetic theory for geophysical applications, In Hansen, D.A., et al (Eds.), *Mining Geophysics*, vol. II, Theory, (pp.10-198), Soc. of Exploration Geophysicists, Tulsa, Oklahoma. doi: **https://doi.org/10.1190/1.9781560802716.ch2**

Ward, S. H. (1990). Resistivity and Induced Polarization methods, In Ward, S. H. (Ed.), *Geotechnical and Environmental Geophysics*, vol. I: Review and Tutorial, (pp. 147-189), Soc. of Exploration Geophysicists, Tulsa, Oklahoma. doi: **https://doi.org/10.1190/1.9781560802785.ch6**

Wilkinson, P. B., Loke, M. H., Meldrum, P. I., Chambers, J. E., Kuras, O., Gunn, D. A., and Ogilvy, R. D. (2012). Practical aspects of applied optimized survey design for electrical resistivity tomography, *Geophysical Journal International*, 189, 428-440. doi: **https://doi.org/10.1111/j.1365-246X.2012.05372.x**

Wilkinson, P. B., Meldrum, P. I., Chambers, J. E., Kuras, O., and Ogilvy, R. D. (2006). Improved strategies for the automatic selection of optimized sets of electrical resistivity tomography measurement configuration, *Geophysical Journal International*, 167(3), 1119-1126. doi: **https://doi.org/10.1111/j.1365-246X.2006.03196.x**

Xiao, L.-L., Wei, J.-C., Niu, C., Shi, L.-Q., Zhai, P.-H., Yin, H.-Y., and Xie, D.-L. (2015). Study on the distortion of apparent resistivity curves caused by the ¨infinite¨ electrode space of a Pole-Pole array and its correction, *Journal of Applied Geophysics*, 118, 124-138. doi: **https://doi.org/10.1016/j.jappgeo.2015.04.014**

Zhou, B., and Dahlin, T. (2003). Properties and effects of measurement errors on 2D resistivity imaging surveying, *Near Surface Geophysics*, 1(3), 105-117. doi: **https://doi.org/10.3997/1873-0604.2003001**